

UKAEA-CCFE-PR(20)107

A. Fernandez-Caballero, E. Bousser, S.M. Shubeita,
P.T. Wady, Y.Gue, Ram Krishna, M. Gorley, D.
Nguyen-Manh, P. M. Mummery, E.J. Pickering

High-dose ion irradiation damage in Fe₂₈Ni₂₈Mn₂₆Cr₁₈ characterised by TEM and depth-sensing nanoindentation

Enquiries about copyright and reproduction should in the first instance be addressed to the UKAEA Publications Officer, Culham Science Centre, Building K1/O/83 Abingdon, Oxfordshire, OX14 3DB, UK. The United Kingdom Atomic Energy Authority is the copyright holder.

The contents of this document and all other UKAEA Preprints, Reports and Conference Papers are available to view online free at scientific-publications.ukaea.uk/

High-dose ion irradiation damage in Fe₂₈Ni₂₈Mn₂₆Cr₁₈ characterised by TEM and depth-sensing nanoindentation

A. Fernandez-Caballero, E. Bousser, S.M. Shubeita, P.T. Wady, Y.Gue, Ram Krishna, M. Gorley, D. Nguyen-Manh, P. M. Mummery, E.J. Pickering

High-dose ion irradiation damage in $\text{Fe}_{28}\text{Ni}_{28}\text{Mn}_{26}\text{Cr}_{18}$ characterised by TEM and depth-sensing nanoindentation

A. Fernández-Caballero^{a,b,c}, E. Bousser^{d,e}, S.M. Shubeita^f, P.T. Wady^f, Y. Gu^{e,g}, Ram Krishna^e, M. Gorley^b, D. Nguyen-Manh^b, P. M. Mummery^c, E. J. Pickering^e

^a*Department of Engineering Science, University of Oxford, Parks Road, Oxford, OX1 3PJ*

^b*CCFE, United Kingdom Atomic Energy Authority, Abingdon OX14 3DB, UK*

^c*Department of Mechanical Aerospace and Civil Engineering, University of Manchester, Manchester M13 9PL, UK*

^d*Engineering Physics Department, École Polytechnique de Montréal, P.O. Box 6079, Station Centre-ville, Montréal, Québec H3C 3A7, Canada*

^e*Department of Materials, University of Manchester, Manchester M13 9PL, UK*

^f*Dalton Cumbrian Facility, The University of Manchester, Moor Row CA24 3HA, UK*

^g*Swansea University Bay Campus College of Engineering, Crymlyn Burrows, Swansea, SA1 8EN*

Abstract

One of the key challenges for the development of high-performance fusion materials is to design materials capable of maintaining mechanical and structural integrity under the extreme levels of displacement damage, high temperature and transmutation rates. High-entropy alloys (HEAs) and other concentrated alloys have attracted attention with regards to their performance under fusion conditions. In recent years, a number of investigations of the irradiation responses of HEAs have peaked the community's interest in them, such as the work of Kumar et al. [1], who examined $\text{Fe}_{27}\text{Ni}_{28}\text{Mn}_{27}\text{Cr}_{18}$ at doses as high as 10 dpa. In this work, we study $\text{Fe}_{28}\text{Ni}_{28}\text{Mn}_{26}\text{Cr}_{18}$ concentrated multicomponent alloy with irradiation doses as high as 20 dpa. We find the presence of Cr rich bcc precipitates in both the un-irradiated and in the irradiated condition, and the presence of dislocation loops only in the irradiated state. We correlate the features found with irradiation hardening by the continuous stiffness method (CSM) depth-sensing nanoindentation technique and see that the change in the bulk hardness increases significantly at 20 dpa

for temperatures 450 °C. These results indicate that the alloy is neither stable as a single phase after annealing at 900 °C, nor particularly resistant to irradiation damage, as have been previously claimed.

Keywords: CrFeMnNi, self-ion irradiation, STEM-EDX, XRD, depth-sensing nanoindentation

1. Introduction

Alloys containing five or more elements in nearly equal atomic concentration or with more than 5 % concentration crystallising have been referred as high entropy alloys after Yeh et al. [2, 3] or as multi-component alloys (MCPs) after Cantor [4]. The high number of different combinations of elements in concentrated multicomponent alloys can make possible the discovery of materials properties that can not be achieved in conventional alloys, which typically contain one principal element. The interest of concentrated multicomponent alloys as high-temperature structural materials for nuclear industries has been motivated by some reports of attractive mechanical properties at elevated temperatures including hardness, strength, ductility, wear, and radiation and corrosion resistance [5].

The structural materials for fusion reactors plants will experience very demanding environments in terms of high temperatures (300-800 °C) and intense 14 MeV neutron irradiation fluxes [6] posing potential challenges to mechanical strength, fracture toughness and ductility and dimensional changes due to void swelling and creep [7]. The development of high-performance materials that are radiation resistant is critical for advanced nuclear reactor systems. Due to their chemical complexity, different atomic sizes and charge transfer among the elements in the random solid solution of concentrated multicomponent alloys, atomic-level stresses have been rationalised as the cause for reduced number densities of vacancy or interstitial defect clusters due to enhanced vacancy-interstitial recombination of defect clusters in the cascade following the thermal spike after irradiation by high energy particles [8, 9, 10].

Recently, attention has been drawn to concentrated multicomponent alloys, in particular, containing light transition metal elements Co, Cr, Fe, Ni, and Mn that form predominantly a single phase with secondary phase precipitates after prolonged heat treatments [4, 11]. For some of the alloys belonging to the family of CrMnFeCoNi but without Co, mechanical tensile

31 tests have indicated that these alloys can become brittle due to the presence
32 of the hard and brittle σ phase [11, 12]. The embrittlement studies motivated
33 the study of particular alloy compositions, specifically Cr content controlled
34 to narrow down selection to composition $\text{Fe}_{28}\text{Ni}_{28}\text{Mn}_{26}\text{Cr}_{18}$ [13]. The com-
35 position of $\text{Fe}_{28}\text{Ni}_{28}\text{Mn}_{26}\text{Cr}_{18}$ is also favoured for nuclear applications due to
36 the removal of Co. If Co is exposed to intense high energy neutron fluxes, it
37 can transmute into ^{60}Co long-lived radioactive isotope [14].

38 In previous work [1], the microstructure and hardness of 5.8 MeV Ni ir-
39 radiated $\text{Fe}_{27}\text{Ni}_{28}\text{Mn}_{27}\text{Cr}_{18}$ concentrated multicomponent alloy was studied
40 up to doses of 10 dpa and temperatures of 700 °C by TEM and by depth-
41 sensing nanoindentation. In the study, the concentrated multicomponent
42 alloy was reported to be a single-phase solid solution and remain stable dur-
43 ing irradiation. The essential radiation-induced features were high density
44 dislocation loops, reduced grain boundary Cr and Fe and increased Ni seg-
45regation compared to FeCrNi austenitic stainless steels irradiated to similar
46 doses, and lack of void formation. The authors rationalised the small size,
47 and high number density of dislocation loops in comparison to equivalent
48 irradiated FeCrNi austenitic stainless steels as being due to a reduced point
49 defect recombination in this concentrated multicomponent alloy.

50 Heavy-ion irradiations have been used as simulation experiments for neu-
51 tron damage in structural materials since they are amenable to flexible en-
52 vironmental conditions, including control of temperature and displacement
53 per atom rate [15]. These parameters are not so easily controlled during in-
54 reactor irradiation experiments. Furthermore, the high rates of displacement
55 per atom from heavy ion irradiations, which are several orders of magnitude
56 higher than for neutron irradiation, speed up the accumulation of radiation
57 damage [15]. The drawbacks of heavy ion irradiation are mainly the few μm
58 ranges of implanted damage depth that makes difficult sample preparation
59 for microscopy.

60 This current work aimed to assess the irradiation behaviour of the $\text{Fe}_{28}\text{Ni}_{28}$
61 $\text{Mn}_{26}\text{Cr}_{18}$ alloy in detail at high doses to further confirm the apparent irra-
62 diation resistance of the alloy. The structure of this paper is as follows: In
63 section 2 the experimental methods for the thermomechanical processing of
64 the sample preparation, the self-ion irradiation, the depth-sensing nanoin-
65 dentation and TEM sample preparation are described; In section 3 the mi-
66 crostructure of $\text{Fe}_{28}\text{Ni}_{28}\text{Mn}_{26}\text{Cr}_{18}$ is characterized in un-irradiated state by
67 TEM, then the microstructure of the 5 MeV Ni irradiated $\text{Fe}_{28}\text{Ni}_{28}\text{Mn}_{26}\text{Cr}_{18}$
68 is characterized by TEM, and then hardening is studied from depth-sensing

69 nanoindentation measurements.

70 2. Experimental methods

71 2.1. Thermo-mechanical processing and sample preparation

72 The $\text{Fe}_{28}\text{Ni}_{28}\text{Mn}_{26}\text{Cr}_{18}$ concentrated multicomponent alloy specimens were
73 prepared by arc melting in a Ti-gettered high-purity argon atmosphere by
74 mixing high purity (99.9%) elemental Cr, Mn, Fe and Ni in the concentra-
75 tion of 18%-27%-27%-28% at. % respectively. The ingots were flipped and
76 remelted several times during the arc melting process ¹. To cross-check the
77 average chemical composition of the as-cast concentrated multicomponent
78 alloys analysis with a FEI Quanta 650 SEM (Scanning Electron Microscope)
79 Oxford instruments EDX (Energy Dispersive X-rays) was conducted over 10
80 regions of the approximate area of 100 μm by 100 μm . The resulting analysis
81 is shown in Table 1, which agrees reasonably well with the expected compo-
82 sition values, thus indicating that no relative depletion of any alloy element
83 in bulk occurred in the manufacturing process.

Table 1: Chemical composition of $\text{Fe}_{28}\text{Ni}_{28}\text{Mn}_{26}\text{Cr}_{18}$ concentrated multicomponent alloys for this work, measured with SEM-EDX

Element	wt.% ([1])	wt.% (this work)	at.% (this work)
Cr	18	16.7 ± 0.3	18.0 ± 0.1
Mn	27	25.6 ± 0.6	26.0 ± 0.6
Fe	27	28.1 ± 0.5	28.1 ± 0.3
Ni	28	29.3 ± 0.5	27.9 ± 0.3

84 More detailed analysis performed with EDX revealed micro-segregation
85 at the μm scale with the presence of dendrite-like structures of approximately
86 20 μm separated see Figs. 1 (a)-(d). To homogenise and anneal possible sinks
87 for irradiation defects in the microstructure we performed a homogenization
88 heat treatment at 1200 °C for 48 hr and water quench, then deformed in
89 an uniaxial compression to a thickness reduction of 40%. And finally a re-
90 crystallisation heat treatment at 900 °C for 4 hr followed by furnace cooling.
91 The results are shown in Figs. 1 (e)-(h) The heat treatment was performed
92 to reproduce work by Kumar et al. [1].

¹The samples were prepared at the University of Sheffield

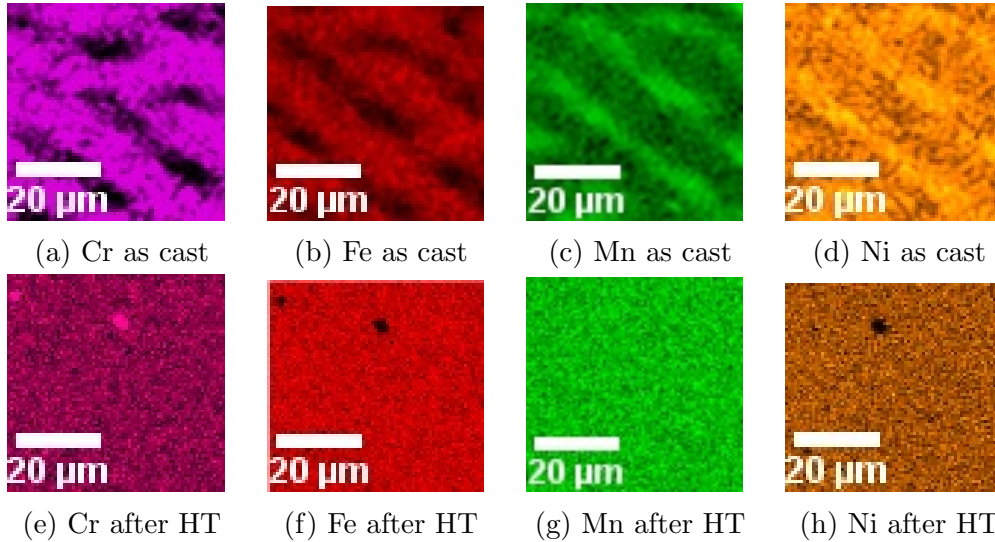


Figure 1: Representative SEM EDX maps of Cr, Fe, Mn and Ni before a-d and after e-h homogenisation heat treatment in as cast $\text{Fe}_{28}\text{Ni}_{28}\text{Mn}_{26}\text{Cr}_{18}$ concentrated multicomponent alloys at $1200\text{ }^{\circ}\text{C}$ for 48 hrs. During the homogenization and recrystallization heat treatments MnCr oxide inclusions appeared, these are shown in the heat treated maps as black dots.

93 Thermomechanically processed specimens were electro-discharge machined
 94 into square blocks of approximate size 10 mm and thickness between 0.5 and
 95 1 mm. Grinding and polishing were performed on an automatic spinner
 96 platen with abrasive SiC paper P800, P1200, P2400 and P4000, then fol-
 97 lowed by polishing with $1\text{ }\mu\text{m}$ polycrystalline diamond suspension in a cloth,
 98 and finally the specimens were OPS polished until grain boundaries appeared
 99 slightly etched in the optical microscope Zeiss Axio. The mean grain size in
 100 the recrystallised condition was found to be approximately $31 \pm 9\mu\text{m}$ by using
 101 a simple linear intercept method from the SEM micrograph in Fig. 2 a

102 The recrystallised condition was characterised by X-ray diffraction (XRD)
 103 to ascertain that the crystal structure is face-centred cubic (fcc) and to find
 104 the lattice spacing. The powder diffractometer used for this work was a
 105 Phillips XRD PANalytical X'Pert Pro using a combined characteristic radi-
 106 ation of $\text{CuK}\alpha_1$ and $\text{CuK}\alpha_2$ X-rays with a Ni foil to remove β X-ray radiation
 107 and a graphite monochromator to reduce fluorescence effects that can mask
 108 the diffraction peaks in samples containing transition metal elements (our
 109 sample has Fe, Cr, Mn and Ni). This diffractometer used the $\theta - 2\theta$ Bragg-

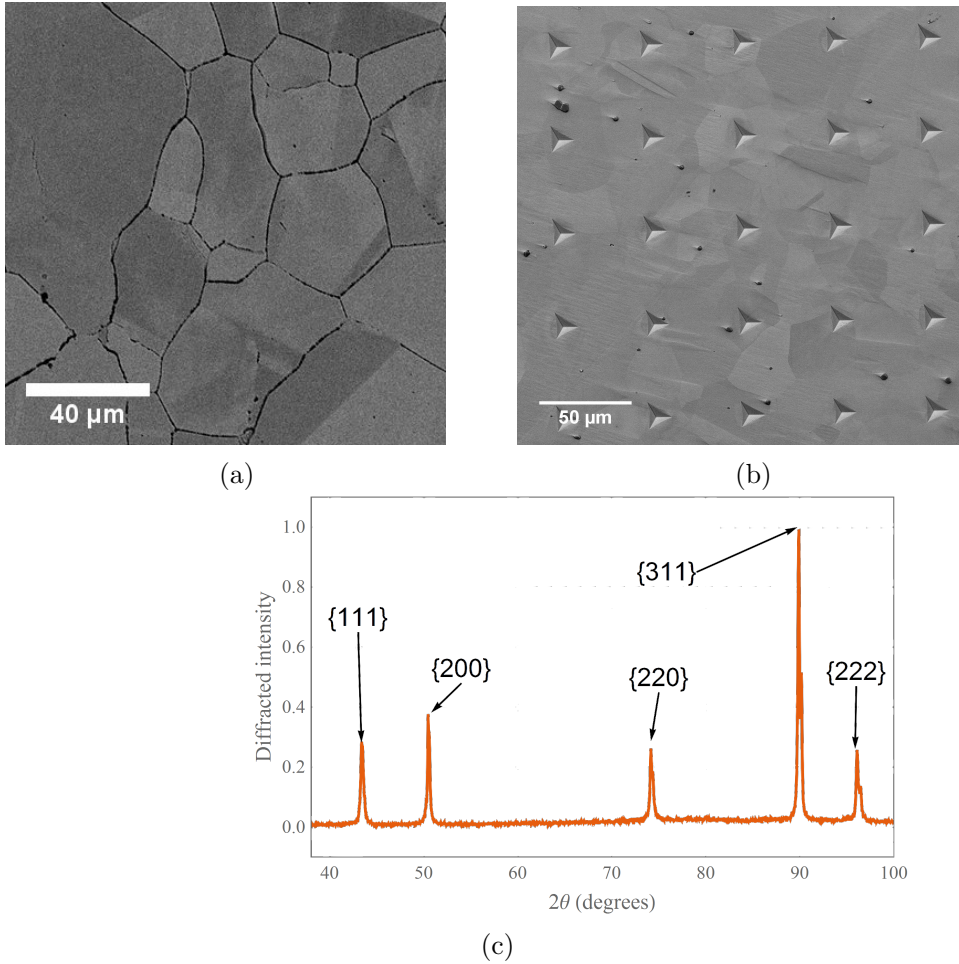


Figure 2: a) SEM Backscattered electron micrograph of the recrystallised microstructure indicating the grain structure after etching with metallographic etchant of nitric acid and ethanol. b) Representative SEM image of array depth-sensing nanoindentation impressions after testing. The impressions are spaced approximately 50 μm apart and were performed on a sample irradiated at 300 $^{\circ}\text{C}$ and 20 dpa. c) XRD diffraction pattern as obtained from recrystallised $\text{Fe}_{28}\text{Ni}_{28}\text{Mn}_{26}\text{Cr}_{18}$ concentrated multicomponent alloy. The secondary peaks to the right of the highest peaks are due to diffraction caused by longer wavelength of $\text{CuK}\alpha_2$ radiation.

110 Brentano geometry, and the sample was spun along the normal to its planar
 111 surface. The working voltage of the diffractometer was 40 kV, and the oper-
 112 ating current was 40 mA. The scanning region ranged from 35 ° to 110 °, in
 113 steps of 0.05°.

114 We use the CMPR software [16] to investigate the parameters of the
 115 structure by predicting the angular location for the diffracted intensities from
 116 basic crystallographic information and optimise the lattice constants to fit
 117 the experimental intensity peak positions.

118 *2.2. Self-ion irradiation experiment*

119 For the irradiation experiment, the recrystallised specimens were mounted
 120 on the sample end-stage at the 30 ° beamline from Dalton Cumbrian Facility
 121 [17]. The beam was focused and operated in rastering mode. The last beam
 122 slits were adjusted to trim the beam to irradiate an area uniformly of 7 by 7
 123 mm² area for all of the samples reported in this study. The sample temper-
 124 ature was monitored continuously throughout the irradiation experiment by
 125 thermal imaging to measure the temperature increase due to the combined
 126 beam heating and external heaters (see Fig. 3 c). The real beam current
 127 on the sample was monitored through the continuous reading of charge de-
 128 posited at the end-stage by a data acquisition system implemented with Lab-
 129 View National Instruments. Corrections were applied to measured current
 130 on the sample to compensate for the spurious secondary electron emission
 131 from the sample upon the impact of the heavy ions.

Table 2: Irradiations performed at Dalton Cumbrian Facility [17] with Nickel ions (excitation state +3) at 5 MeV under different conditions. The dose rate (dpa/s) was 2.4E-04 for all but the 2nd sample in the Table for which was 4.40E-04

Ion fluence (ion/cm ²)	Dose (dpa)	Temperature (°C)	Exposure (time)
8.00E+14	2	300	2 h 19 min
8.00E+15	20	300	12 h 37 min
8.00E+15	20	450	23 h 9 min
8.00E+14	2	450	2 h 19 min
8.00E+13	0.2	450	14 min

132 The displacements per atom (dpa) were estimated from SRIM (2008 ver-
 133 sion) [18] code and at 80% depth of the Bragg peak for 5 MeV Ni ions with

134 +3 charge state. To make consistent our ion irradiation doses with potential
135 future neutron irradiations we set up the SRIM simulation with lattice and
136 surface binding energies of the Cr, Mn, Fe and Ni atoms equal to zero and we
137 choose the Kinchin-Pease calculation mode following findings from [19]. For
138 the displacement energies of the lattice atoms Cr, Fe, Mn and Ni the value
139 40 eV was used [19]. The peak dpa is estimated from SRIM dpa per fluence
140 and the estimated fluence of the ion irradiation deposited charge corrected
141 on each of our specimens (see Fig. 3 a).

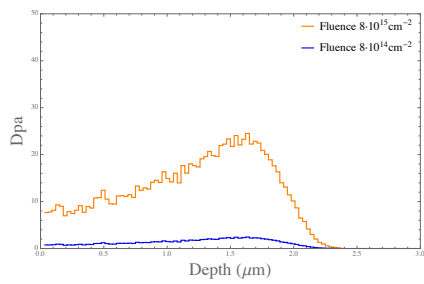
142 The peak dose achieved was approximately 20 dpa, and the peak Ni
143 implantation was approximately 0.14 at.%, as indicated in Figs. 3 a, and b
144 respectively. The values for the main parameters fluence, dose, irradiation
145 temperature, exposure time and dose are detailed in Table 2.

146 *2.3. Depth-sensing nanoindentation methods*

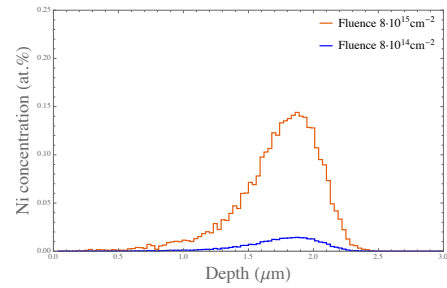
147 For carrying out depth-sensing nanoindentation, we used an MTS Nano
148 Indenter XP equipped with a Berkovich geometry diamond indenter.. The
149 maximum allowed drift rate was set to 0.15 nm/s and a surface approach
150 velocity for the tip of 10 nm/s. The penetration depth examined in the
151 irradiated specimens ranged from 0 to 2000 nm with a maximum load of
152 200 mN. The projected contact area of the tip was evaluated using a fused
153 silica standard material with $E_r=69.6$ GPa and $\nu=0.17$ over a contact depth
154 range from approximately 5 to 1400nm. The average hardness values were
155 determined from averaging 25 hardness values each being derived from a
156 continuous load-displacement curve by using the continuous stiffness method
157 (CSM) using the approach proposed by Oliver and Pharr [20]. The 25 (5x5)
158 impressions were spread in an array of points separated by 50 μm to avoid
159 interference effects due to localised plastic zones among the indents (see Fig.
160 2 b).

161 *2.4. TEM sample preparation*

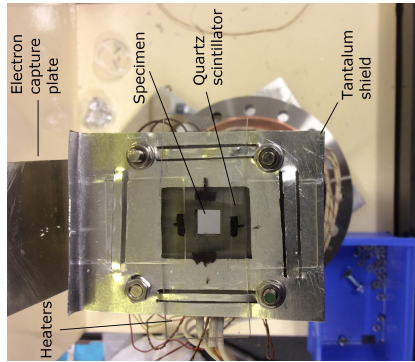
162 TEM lamellae for characterising the 1 μm thin irradiated layer were pre-
163 pared by the FIB lift-out method using Ga ions in an FEI Quanta 3D oper-
164 ated at 30 kV. Final cleaning-polishing was performed at 2 kV to minimise
165 Ga ions induced damage on the microstructure until lamellae were electron
166 transparent. The lamellae were mounted in a Cu TEM grid. The lamel-
167 lae were observed in Tecnai F20, and an FEI Talos F200A with TEM and
168 STEM-EDX modes both operated at the accelerating voltage of 200 kV. The
169 scale bar for diffraction was calibrated by using the fitted lattice spacing for



(a)



(b)



(c)

Figure 3: Displacement per atom (Dpa) (a) and Nickel (atomic %) implantation profile (b) in $\text{Fe}_{28}\text{Ni}_{28}\text{Mn}_{26}\text{Cr}_{18}$ for the two fluences considered in Table. 2 calculated with SRIM [18]. (c) Sample set up for irradiation experiment at beamline of Dalton Cumbrian Facility. An approximate area of 7 by 7 mm² delimited by scintillator quartz crystal is irradiated uniformly by the ion beam. The irradiation temperature is controlled by the heaters below the specimen and a chiller circulating continuously. The tantalum shield prevents the structural material of the stage from becoming activated by the incident radiation

170 fcc structure of the recrystallised condition in the powder diffraction mea-
171 surements.

172 **3. Results and discussion**

173 *3.1. Microstructural characterization in the un-irradiated condition*

174 The XRD pattern from the recrystallised microstructure indicates that
175 the fcc structure is the main phase within the detection limits of the signal-
176 to-noise ratio (Fig. 2 c). The single-phase stability of $\text{Fe}_{28}\text{Ni}_{28}\text{Mn}_{26}\text{Cr}_{18}$
177 concentrated multicomponent alloys is in agreement with the chemical ho-
178 mogeneity colour maps of Cr, Mn, Fe and Ni in the SEM-EDX results after
179 annealing (see Fig. 1). The lattice parameter was found to be 3.610 ± 0.005 Å
180 in space group O_h^5 , this corresponds to the stress free microstructure. A lat-
181 tice parameter of 3.64 Å was found from the alloy of Cr, Mn, Fe and Ni with
182 similar composition in the fcc phase [1]. The relative height of the diffracted
183 intensities is different from that expected by the intrinsic lattice geometrical
184 multiplicities of a randomly oriented aggregate of crystals as typically used
185 in conventional powder diffraction. This is likely to be an indicator of some
186 crystallographic texture resulting from the thermomechanical processing ap-
187 plied.

188 SEM-EDX maps (shown in Fig. 1) and TEM selected area diffraction
189 from the matrix (Fig. 4 c)) material confirmed the XRD predictions of
190 fcc homogeneous solid solution phase except for oxide inclusions abundant
191 in Mn and Cr associated to the spinel structure. Their presence could be
192 related to the oxygen impurities in the raw materials or contamination in
193 the manufacturing process in the arc melter. Similar inclusions have been
194 found for Cantor alloy [21, 11].

195 TEM of the recrystallised alloy revealed precipitates at the grain bound-
196 aries. The precipitates found are shown in Fig. 4 (e)-(i), where the structure
197 of these precipitates is consistent with the bcc symmetry. We also found
198 precipitates within the recrystallised grains in the samples. By calculating
199 the distance between diffraction spots along with the (200) directions (Fig.
200 4 a), the lattice constant of the bcc phase (Fig. 4 b) is approximately 2.9
201 Å. The findings of a bcc phase with very close lattice constant to pure Cr
202 has been reported in previous works for CrMnFeCoNi Cantor alloy [22]. The
203 bcc precipitates are seen to be rich in Cr and depleted in Mn, Fe and Ni as
204 shown in STEM-EDX maps in Fig. 4 e-h.

205 The presence of the bcc phase was not detected in previous studies per-
206 formed with a CrMnFeNi concentrated multicomponent alloy with similar
207 composition to the present work [1]. The phase stability of $\text{Fe}_{27}\text{Ni}_{28}\text{Mn}_{27}\text{Cr}_{18}$
208 concentrated multicomponent alloy has been investigated by first principles
209 DFT cluster expansion and Monte Carlo simulations [23]. The simulations
210 predicted that Cr tetrahedral clusters in the fcc lattice are not thermody-
211 namically favoured and Cr segregation may precipitate into the bcc lattice,
212 which is the ground state of pure Cr. The equimolar CrFeMnNi alloy has
213 been predicted to be two phase (fcc+bcc) from solidification and stable in the
214 temperature range $T > 1000$ K and at lower temperatures two phase (fcc+ σ).
215 After annealing at 1273 K for 6 days, the equimolar CrFeMnNi was found to
216 contain three phases: fcc, bcc, and σ . In particular, the concentration and
217 lattice spacing of the bcc phase was predicted by CALPHAD calculation and
218 measured by XRD and EDS-SEM to reveal a Cr concentration in the range
219 44.2-45.2 at. %, and a lattice spacing of 0.28 nm [24].

220 3.2. Microstructural characterization under irradiation

221 The Bragg peak corresponding to the Ni irradiation was found at the
222 approximate depth of 1.6 μm from SRIM simulations, which according to
223 our estimations from Fig. 3 a is separated from the Ni implantation peak
224 which is at 1.9 μm (see Fig. 3 b).

225 The Cr-rich BCC particles were also observed in the irradiated specimens
226 (see Fig. 5a)). These precipitates are most likely consistent with the BCC
227 phase identified. An oxide phase, also rich in Cr and other elements such
228 as Mn can also be distinguished from the same figure. It is likely that this
229 phase is a spinel phase that was also observed in the un-irradiated specimens.
230 The effect of irradiation in the volume fraction of the precipitates was not
231 ascertained in this study, owing to the difficulties associated with making
232 meaningful volume fraction measurements in the irradiated layer. The role
233 that irradiation plays in these precipitates requires alternative techniques
234 to the FIB used here to sample more irradiated volume and therefore get
235 meaningful precipitate statistics. The findings of the Cr-rich BCC particles
236 in the irradiated condition is in contrast to previously reported work in this
237 alloy [1], which found no precipitates at all.

238 We also observed a NiMn segregated region in the irradiated samples
239 with STEM-EDX maps in the irradiated specimens, but it was not possible
240 to confidently rule out that these formed earlier in the thermo-mechanical
241 processing stage before irradiation. These are shown in Fig. 5c)-5d). The

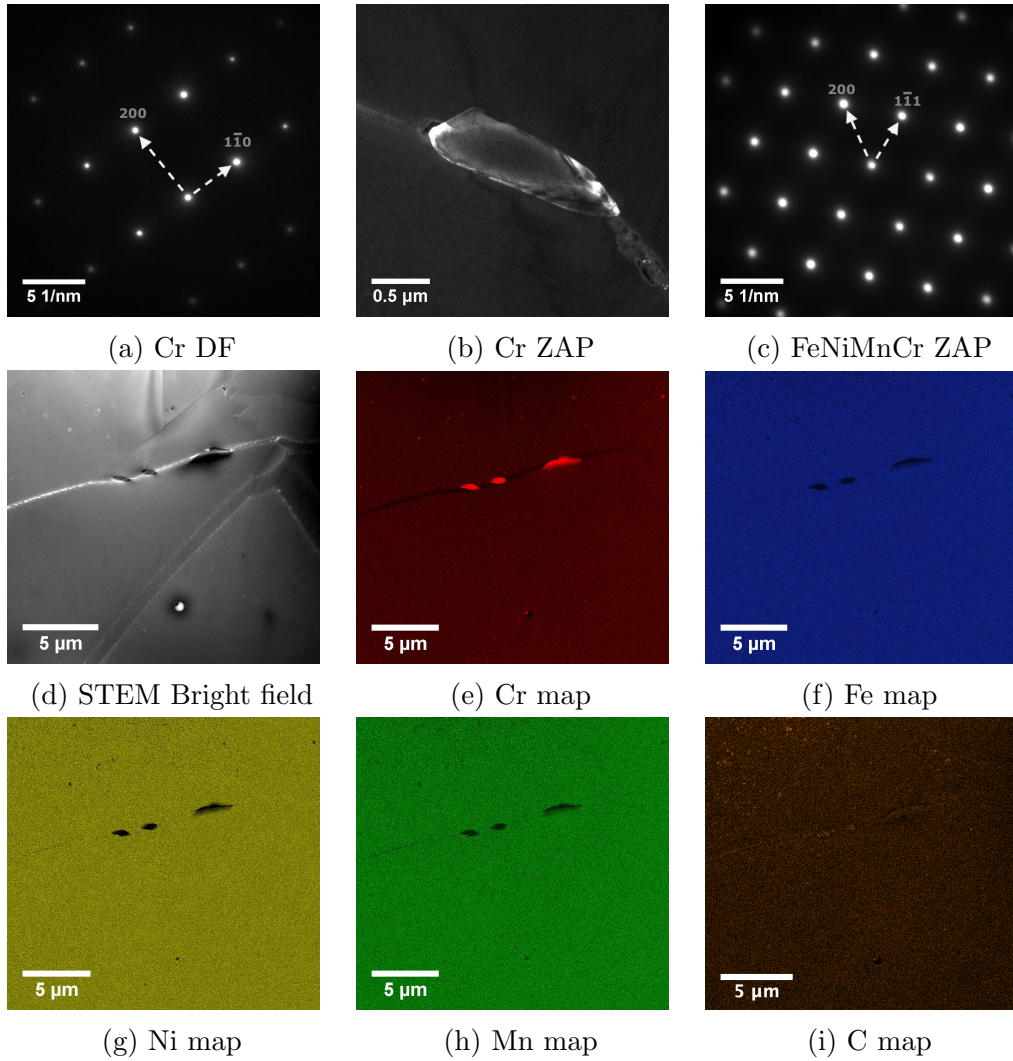


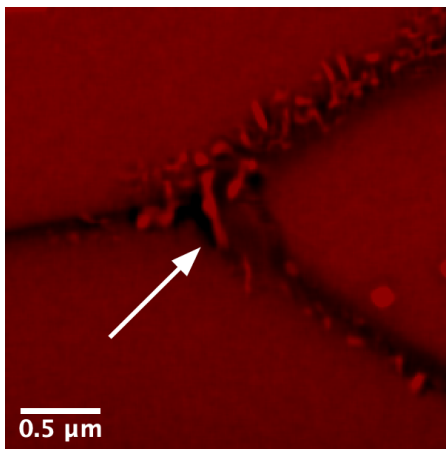
Figure 4: TEM selected area diffraction (the zone axis is $[011]$ crystallographic direction for bcc phases (a), Dark Field Micrographs (b) and fcc phase (c). TEM selected area diffraction (the zone axis is $[011]$ crystallographic direction for the fcc matrix). STEM Bright Field (d), and STEM energy dispersive X-ray maps of Cr (e), Fe (f), Mn (h), Ni (g), and C (i).

242 dimensions of these fine precipitates made it difficult to identify the structure
243 and lattice spacing by selected area diffraction in the TEM. The presence
244 of an L1₀ NiMn phase after ageing at intermediate temperatures has been
245 reported before in similar alloys [22, 25].

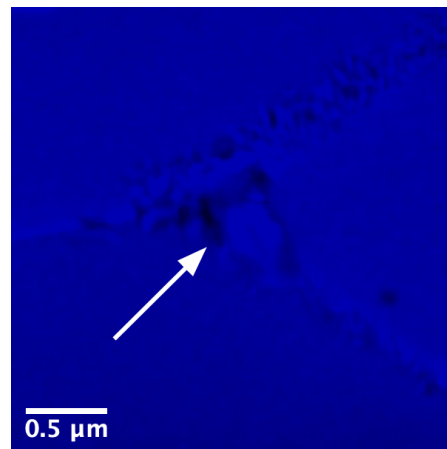
246 Recently, DFT(Density Functional Theory) based cluster expansion and
247 Monte Carlo simulations published by the author have predicted the for-
248 mation of L1₀ MnNi phase in Fe₂₇Ni₂₈Mn₂₇Cr₁₈ [23, 26] at temperatures
249 T<1300 K. Furthermore, simulations for formation L1₂ CrFe₃ in the tem-
250 perature range 500-1200 K were also predicted by the author simulations,
251 however the experimental measurements in this work did not indicate the
252 presence of L1₂ CrFe₃.

253 Voids and dislocation loops were found in pure Ni after self-ion irradiation
254 at doses as high as 13 dpa and temperatures 300-725 °C [27]. Westmore
255 et al reported significant difficulties in measuring the dislocation loop densi-
256 ties due to their dense distribution. They estimated diameters ranging
257 between 44 and 95 Å, and number densities $3.0 \cdot 10^8 - 7.8 \cdot 10^{10} \text{ Å}^{-3}$. In this
258 work, and in agreement with self-ion irradiated studies in a similar composi-
259 tion multicomponent alloy, we found dislocation loops and no voids. In Fig.
260 6 c)-d), we show dislocation loop contrast corresponding to Frank loops by
261 using a two-beam condition ($\mathbf{g} = 220$). In fcc materials, the vacancies and in-
262 terstitials are known to form dislocation loops of vacancy or interstitial types
263 as well as voids. In situations where vacancy mobility is low due to an oper-
264 ating temperature less than approximately half of the melting temperature,
265 vacancy dislocation loops are known [28] to be unstable due to the higher
266 capture radius of dislocation for interstitial than vacancy point defects. Thus
267 resulting in the annihilation of vacancy loops by diffusing interstitial point
268 defects and leaving the only interstitial loops stable. Based on the dislocation
269 bias argument we expect that the loops are of interstitial-type faulting.

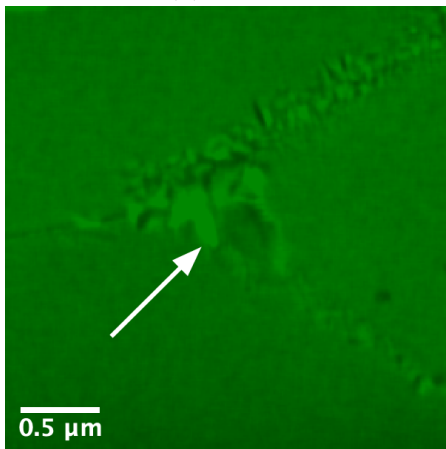
270 Preparation of TEM lamellae using Ga ions with the FIB technique can
271 produce ripple-shaped contrast and black dot contrast [29]. A comparison of
272 the un-irradiated and irradiated specimens shown in Figs. 6 a-b and Figs. 6
273 c-d demonstrates that the damage seen is not a result of FIB preparation;
274 there is no damaged layer in the un-irradiated samples when compared to
275 remaining irradiated samples Figs. 6 (c)-(f) . The Frank loops may there-
276 fore be attributed to the Ni 5 MeV irradiation field and not from the FIB
277 preparation work. The depth of the observed damage layer in the irradiated
278 sample in Fig. 6 d has a varying depth between 1.9 and 2.1 μm is consistent
279 with SRIM 5 MeV Ni implantation and dpa simulations as shown in Figs. 3



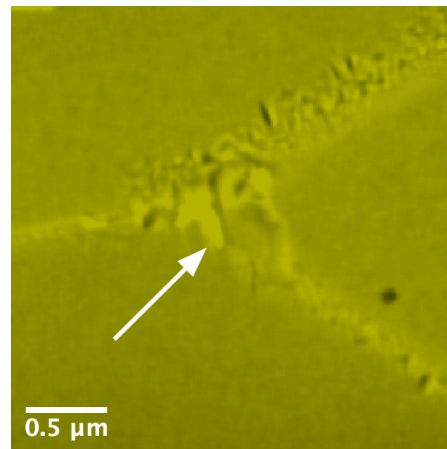
(a) Cr map



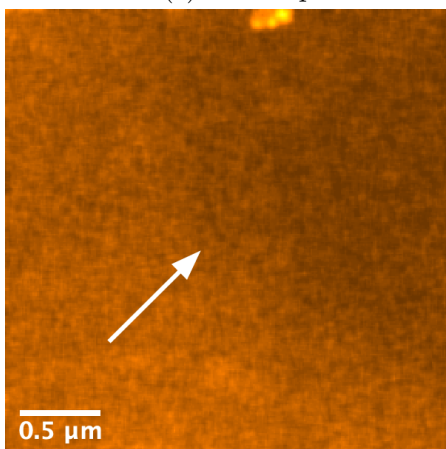
(b) Fe map



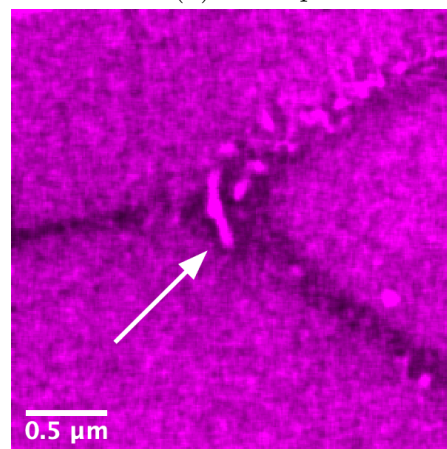
(c) Mn map



(d) Ni map

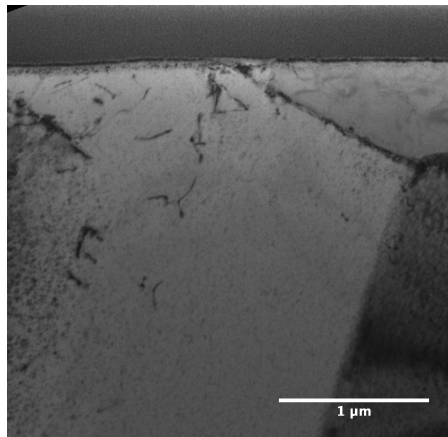


(e) C map

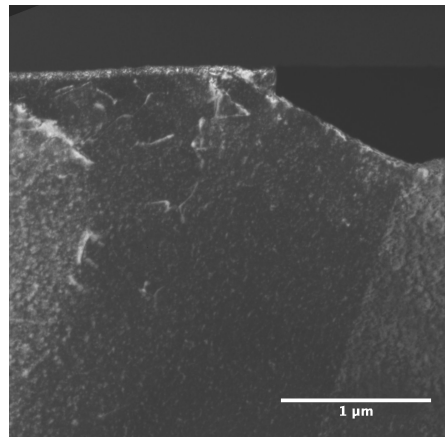


(f) O map

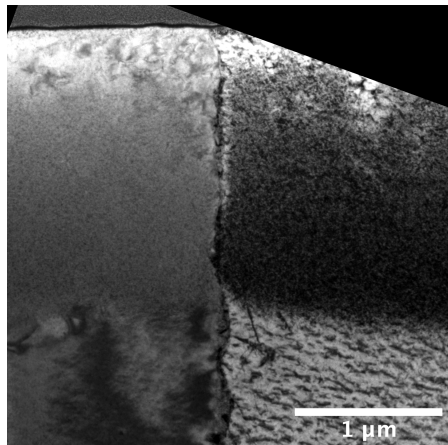
Figure 5: STEM EDX maps of Cr, Fe, Mn, Ni, C, and O at a triple junction. The arrow points to the NiMn phase.



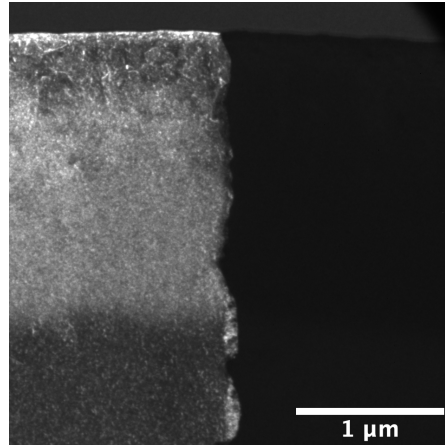
(a) Bright field un-irradiated



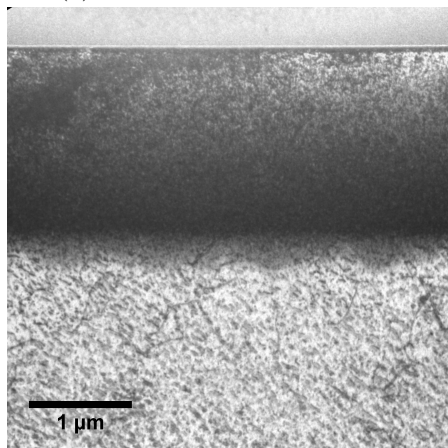
(b) Dark field un-irradiated



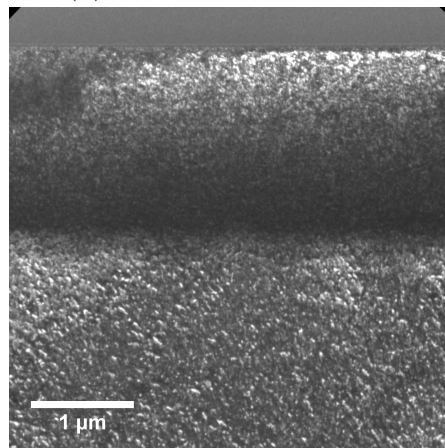
(c) Bright field 2 dpa 450 °C



(d) Dark field 2 dpa 450 °C



(e) Bright field 20 dpa 450 °C



(f) Dark field 20 dpa 450 °C

Figure 6: Micrographs of un-irradiated a)-b) and irradiated concentrated multicomponent alloys lamella prepared by the FIB lift-out method c)-f). In the lamellae, the platinum layer of protection is found at the top of the images. The platinum location indicates the entry direction of the ion irradiation as it penetrated the bulk of the recrystallised specimen. In Fig. (c) the half grain in the top left corner is cut off due to the image rotation in the TEM.

280 a and (b)

281 3.3. Irradiation hardening from depth-sensing nanoindentation tests

282 Bulk equivalent hardness in irradiated specimens, H_0 , is computed from
283 fitting the contact depth-dependent hardness $P[h_c]/A_c[h_c]$. The hardness
284 plots are shown in Fig. 7 a) and b). Several models for irradiation hardening
285 have been reported in the literature [30], the simplest one being Kasada
286 two parameter model[31]. The hardness- contact depth plots were fitted to
287 Kasada's film/substrate model in terms of parameters h_0 and H_0 similar to
288 the Nix-Gao indentation size effect (ISE) [32], $H[h_c] = H_0\sqrt{1 + h_0/h_c}$. The
289 inflection point in the hardness envelope plots of the irradiated samples can
290 be observed from Figs. 7 a) and b). The inflection points in (0.2, 20 dpa
291 for 450C and 2, 20 dpa for 300C) are approximately located at 200 nm.
292 This sets the upper end for fitting of the data to Kasada's model, $H[h_c] =$
293 $H_0\sqrt{1 + h_0/h_c}$, which was approximately given by $3 < 1/h_c < 10$ (see Fig.
294 7 c)-d)). Note that this range for data fitting is approximately consistent
295 with similar ion-irradiated specimens [31, 33], and that the hardness squared
296 curve for the non-irradiated curve in the corresponding range fits to a straight
297 line (see 7 e)) as in Nix-Gao model. The dashed lines in Figs. 7 c) and d)
298 correspond to the fitting of the data to Kasada's film/substrate model. The
299 intercept of this lines with the vertical axis determines H_0^{irr} . The curve for
300 2 dpa at 450 °C is not really showing the inflection point. This could be a
301 material issue or an irradiation issue. Bulk equivalent irradiation hardening
302 in the damaged layer of self-ion implantation is then estimated by subtracting
303 the equivalent bulk hardness of the un-irradiated specimens from the each of
304 the bulk-equivalent hardness in the irradiated samples i.e. $\Delta H_{irr} = H_0^{irr} -$
305 H_0^{nonirr} . These irradiation hardening quantities are obtained from the fits in
306 Fig. 7 c)-d) and the numerical values are indicated in Table 3 as a function
307 of dose and irradiation temperature.

308 From the irradiation hardening $\Delta H_{irr} = H_0^{irr} - H_0^{nonirr}$ for each of the
309 irradiated samples in table 3 we find that hardness increases with dose up to
310 4 GPa at all irradiation temperatures. Furthermore we find that irradiation
311 temperature effects from 300 and 450 °C resulted in no significant change in
312 the irradiation hardening. Kumar et al [1] reported room temperature and
313 500 °C depth-sensing nanoindentation results in ion-irradiated CrMnFeNi.
314 We have compared their data to ours in Table 3. In this work, we explored
315 high doses to 20 dpa, and find that the increase in hardness after irradiation at
316 450 °C is 4.4 GPa, which expands the knowledge of the irradiation behaviour

317 of this alloy after the hardness increase value of 0.47 GPa reported in [1] after
318 3 dpa of irradiation. The error bar magnitude difference for the low dose data
319 at 300 °C of 0.9 is attributed to scatter and difficulty to fit the data. The
320 remaining samples showed less scatter in the data, and the error bar could
321 be reduced to less than 0.7 GPa.

322 Self-ion irradiation in Ni has primarily been focused in void swelling [27],
323 and to the best of our knowledge there are no data with increase in hard-
324 ening data from dislocation loops in pure nickel. Recently, Voyevodin et al.
325 performed 1.4 MeV Ar ion irradiations in a multicomponent CrFeMnNi alloy
326 (with composition 20, 40, 20, 20 *wt.*% respectively) to investigate the radia-
327 tion behaviour by nanoindentation [33]. They have shown that the increasing
328 in hardness measured from continuous stiffness depth-sensing nanoindenta-
329 tion followed by fitting to Kasada method [31] in the CrFeMnNi were 0.75, 1.0
330 ,and 1.25 GPa after 0.3, 1 and 5 dpa of Ar ion irradiations. They also showed
331 that if the multicomponent alloy CrFeMnNi contained a dispersed oxide the
332 increase in hardness could reach higher magnitudes than the precipitate free
333 irradiated samples.

334 The effect of Cr-rich precipitates dispersed in the matrix of CrMnFeNi
335 concentrated multicomponent alloy is expected to contribute to work hard-
336 ening when compared precipitate free condition approximately as the square
337 root of the precipitate volume fraction. The powder diffraction limiting res-
338 olution is estimated to 5% volume fraction. Our XRD analysis could not
339 detect the presence of the Cr-rich precipitate particles in the concentrated
340 multicomponent alloys (Fig. 2 c), and the TEM analysis could evaluate the
341 presence of not more than 1 or 2 Cr-rich precipitates overall (Fig. 4 b).
342 Therefore the expected contribution to work hardening in CrMnFeNi con-
343 centrated multicomponent alloy by the Cr-rich precipitates is estimated to
344 be negligible and independent of irradiation. A more accurate evaluation
345 of the role of irradiation in the precipitate volume fraction would require
346 alternative techniques in between XRD, and TEM.

347 4. Conclusion

348 In the un-irradiated condition, we find Cr-rich bcc precipitates in the
349 fcc- $\text{Fe}_{28}\text{Ni}_{28}\text{Mn}_{26}\text{Cr}_{18}$ concentrated multicomponent alloy matrix, in contrast
350 to previously reported work in this alloy [1], which found no precipitates
351 in any condition. In the irradiated state we find that dislocation loops of
352 interstitial-type occur under irradiation, but in very high number densities

Table 3: Irradiation hardening (in GPa units) concerning non-irradiate condition as obtained from this work (first two rows), and previous work [1] (last two columns). The un-irradiated samples had a reference hardness of 2.6 ± 0.2 GPa

Irradiation temperature (° C)	Low dose (0.2 dpa)	Medium dose (2 dpa)	High dose (20 dpa)
300		2.5 ± 0.9	3.7 ± 0.4
450	0.5 ± 0.5	0.3 ± 0.2	4.4 ± 0.7

	Low dose (0.3 dpa)	Medium dose (3 dpa)
25	2.31 ([1])	
500	0.33 ([1])	0.47 ([1])

353 making quantitative analysis difficult. The TEM experimental observation
 354 of a damaged layer with depth varying between 1.9 and 2.1 μm is consistent
 355 with SRIM 5 MeV Ni implantation and dpa simulations. To understand the
 356 implications of these radiation-induced defects in concentrated multicompo-
 357 nent alloys we use a hardening model based on previous work to convert
 358 measured depth-sensing nanoindentation hardness in the damaged layer of
 359 thickness 1400 nm to bulk equivalent hardness. Change in hardness is mea-
 360 sured at 0.2, 2, and 20 dpa and at irradiation temperatures of 300 °C and
 361 450 °C. The findings of this work suggest that irradiation hardening at 20
 362 dpa is as high as 4 GPa. As a conclusion, it is found that at a very high dose,
 363 the effect of irradiation hardening is not significant in the CrFeMnNi multi-
 364 component concentrated alloy, and the alloy is not stable to precipitation of
 365 secondary Cr-rich bcc phase.

366 5. Supplementary material

367 5.1. Deformation microstructure after recrystallization

368 We find significant dislocation pile-up and dislocation arrays in Figs. 8
 369 a-b in the recrystallised microstructure before irradiation, indicating a build-
 370 up of stress at the phase boundaries between fcc grains or fcc-bcc boundaries.
 371 This is likely to occur from the sample preparation procedure of electropol-
 372 ishing.

373 *5.2. depth-sensing nanoindentation*

374 Excel files with depth-sensing nanoindentation data.
375 Nothing else here?

376 **6. Acknowledgements**

377 A.F.-C. acknowledges assistance with the samples irradiation process to
378 Octav Ciuca (Department of Materials, University of Manchester). This re-
379 search was funded by the Euratom research and training programme 20142019
380 under Grant Agreement No. 633053 and by the Research Council UK (RCUK)
381 Energy Programme (Grant Number EP/P012450/1). The views and opinions
382 expressed herein do not necessarily reflect those of the European Commis-
383 sion. A.F.-C. was funded by the EPSRC grant (EP/L01680X/1) through the
384 Materials for Demanding Environments Center for Doctoral Training

385 **7. References**

- 386 [1] N. K. Kumar, C. Li, K. Leonard, H. Bei, S. Zinkle, Microstructural
387 stability and mechanical behavior of FeNiMnCr high entropy alloy under
388 ion irradiation, *Acta Materialia* 113 (2016) 230–244.
- 389 [2] J. W. Yeh, S. K. Chen, S. J. Lin, J. Y. Gan, T. S. Chin, T. T. Shun,
390 C. H. Tsau, S. Y. Chang, Nanostructured high-entropy alloys with
391 multiple principal elements: Novel alloy design concepts and outcomes,
392 *Advanced Engineering Materials* 6 (2004) 299–303.
- 393 [3] M. C. Tropsky, J. R. Morris, M. Daene, Y. Wang, A. R. Lupini,
394 G. M. Stocks, Beyond Atomic Sizes and Hume-Rothery Rules: Under-
395 standing and Predicting High-Entropy Alloys, *JOM* 67 (2015) 2350–
396 2363.
- 397 [4] B. Cantor, I. Chang, P. Knight, A. Vincent, Microstructural devel-
398 opment in equiatomic multicomponent alloys, *Materials Science and*
399 *Engineering: A* 375-377 (2004) 213–218.
- 400 [5] Y. Zhang, T. T. Zuo, Z. Tang, M. C. Gao, K. a. Dahmen, P. K. Liaw,
401 Z. P. Lu, Microstructures and properties of high-entropy alloys, *Progress*
402 *in Materials Science* 61 (2014) 1–93.

- 403 [6] S. Zinkle, G. Was, Materials challenges in nuclear energy, *Acta Materi-*
404 *alia* 61 (2013) 735–758.
- 405 [7] D. Stork, S. Zinkle, Introduction to the special issue on the technical
406 status of materials for a fusion reactor, *Nuclear Fusion* 57 (2017) 092001.
- 407 [8] C. Lu, L. Niu, N. Chen, K. Jin, T. Yang, P. Xiu, Y. Zhang, F. Gao,
408 H. Bei, S. Shi, M.-R. He, I. M. Robertson, W. J. Weber, L. Wang, En-
409 hancing radiation tolerance by controlling defect mobility and migration
410 pathways in multicomponent single-phase alloys, *Nature Communica-*
411 *tions* 7 (2016) 13564.
- 412 [9] T. Egami, W. Guo, P. D. Rack, T. Nagase, Irradiation Resistance of
413 Multicomponent Alloys, *Metallurgical and Materials Transactions A* 45
414 (2014) 180–183.
- 415 [10] T. Egami, M. Ojha, O. Khorgolkhuu, D. M. Nicholson, G. M. Stocks,
416 Local Electronic Effects and Irradiation Resistance in High-Entropy Al-
417 loys, *Jom* 67 (2015) 2345–2349.
- 418 [11] E. J. Pickering, N. G. Jones, High-entropy alloys: a critical assessment of
419 their founding principles and future prospects, *International Materials*
420 *Reviews* 61 (2016) 183–202.
- 421 [12] N. D. Stepanov, D. G. Shaysultanov, M. A. Tikhonovsky, G. A. Sal-
422 ishchev, Tensile properties of the Cr-Fe-Ni-Mn non-equiatomic multi-
423 component alloys with different Cr contents, *Materials and Design* 87
424 (2015) 60–65.
- 425 [13] Z. Wu, H. Bei, Microstructures and mechanical properties of composi-
426 tionally complex Co-free FeNiMnCr 18 FCC solid solution alloy, *Mate-*
427 *rials Science and Engineering: A* 640 (2015) 217–224.
- 428 [14] E. Bloom, R. Conn, J. Davis, R. Gold, R. Little, K. Schultz, D. Smith,
429 F. Wiffen, Low activation materials for fusion applications, *Journal of*
430 *Nuclear Materials* 122 (1984) 17–26.
- 431 [15] C. Abromeit, Aspects of simulation of neutron damage by ion irradiation,
432 *Journal of Nuclear Materials* 216 (1994) 78–96.
- 433 [16] B. Toby, Program CMPR, NIST, version 1.34 edition, 2005.

- 434 [17] P. Wady, A. Draude, S. Shubeita, A. Smith, N. Mason, S. Pimblott,
435 E. Jimenez-Melero, Accelerated radiation damage test facility using
436 a 5MV tandem ion accelerator, Nuclear Instruments and Methods in
437 Physics Research Section A: Accelerators, Spectrometers, Detectors and
438 Associated Equipment 806 (2016) 109–116.
- 439 [18] J. F. Ziegler, M. Ziegler, J. Biersack, SRIM The stopping and range
440 of ions in matter (2010), Nuclear Instruments and Methods in Physics
441 Research Section B: Beam Interactions with Materials and Atoms 268
442 (2010) 1818–1823.
- 443 [19] R. Stoller, M. Toloczko, G. Was, A. Certain, S. Dwaraknath, F. Gar-
444 ner, On the use of SRIM for computing radiation damage exposure,
445 Nuclear Instruments and Methods in Physics Research Section B: Beam
446 Interactions with Materials and Atoms 310 (2013) 75–80.
- 447 [20] W. Oliver, G. Pharr, An improved technique for determining hardness
448 and elastic modulus using load and displacement sensing indentation
449 experiments, 1992.
- 450 [21] F. Otto, Y. Yang, H. Bei, E. George, Relative effects of enthalpy and
451 entropy on the phase stability of equiatomic high-entropy alloys, *Acta*
452 *Materialia* 61 (2013) 2628–2638.
- 453 [22] F. Otto, A. Dlouhý, K. G. Pradeep, M. Kuběnová, D. Raabe, G. Eggeler,
454 E. P. George, Decomposition of the single-phase high-entropy alloy CrM-
455 nFeCoNi after prolonged anneals at intermediate temperatures, *Acta*
456 *Materialia* 112 (2016) 40–52.
- 457 [23] A. Fernández-Caballero, M. Fedorov, J. Wróbel, P. Mummery,
458 D. Nguyen-Manh, Configurational Entropy in Multicomponent Alloys:
459 Matrix Formulation from Ab Initio Based Hamiltonian and Application
460 to the FCC Cr-Fe-Mn-Ni System, *Entropy* 21 (2019) 68.
- 461 [24] G. Bracq, M. Laurent-Brocq, L. Perrière, R. Pirès, J. M. Joubert,
462 I. Guillot, The fcc solid solution stability in the Co-Cr-Fe-Mn-Ni multi-
463 component system, *Acta Materialia* 128 (2017) 327–336.
- 464 [25] M. E. Bloomfield, K. A. Christofidou, N. G. Jones, Effect of Co on
465 the phase stability of CrMnFeCoxNi high entropy alloys following long-

- 466 duration exposures at intermediate temperatures, *Intermetallics* 114
467 (2019).
- 468 [26] M. Fedorov, J. S. Wróbel, A. Fernández-Caballero, K. J. Kurzydłowski,
469 D. Nguyen-Manh, Phase stability and magnetic properties in fcc fe-cr-
470 mn-ni alloys from first-principles modeling, *Phys. Rev. B* 101 (2020)
471 174416.
- 472 [27] J. E. Westmoreland, J. A. Sprague, F. A. Smidt, P. R. Malmberg, Dose
473 rate effects in nickel ion irradiated nickel, *Radiation Effects* 26 (1975)
474 1–16.
- 475 [28] D. Olander, Fundamental aspects of nuclear reactor fuel elements, U.S.
476 Department of Energy, 1976.
- 477 [29] H.-H. Jin, C. Shin, J. Kwon, Fabrication of a TEM sample of ion-
478 irradiated material using focused ion beam microprocessing and low-
479 energy Ar ion milling, *Journal of Electron Microscopy* 59 (2010) 463–
480 468.
- 481 [30] X. Xiao, L. Yu, Nano-indentation of ion-irradiated nuclear structural
482 materials: A review, *Nuclear Materials and Energy* 22 (2020) 100721.
- 483 [31] R. Kasada, Y. Takayama, K. Yabuuchi, A. Kimura, A new approach to
484 evaluate irradiation hardening of ion-irradiated ferritic alloys by nano-
485 indentation techniques, *Fusion Engineering and Design* 86 (2011) 2658–
486 2661.
- 487 [32] W. D. Nix, H. Gao, Indentation size effects in crystalline materials:
488 a law for strain gradient plasticity, *J. Mech. Phys. Solids* 46 (1998)
489 41–425.
- 490 [33] V. N. Voyevodin, S. A. Karpov, G. D. Tolstolutsкая, M. A.
491 Tikhonovsky, A. N. Velikodnyi, I. E. Kopanets, G. N. Tolmachova,
492 A. S. Kalchenko, R. L. Vasilenko, I. V. Kolodiy, Effect of irradiation on
493 microstructure and hardening of CrFeNiMn high-entropy alloy and its
494 strengthened version, *Philosophical Magazine* 100 (2020) 822–836.

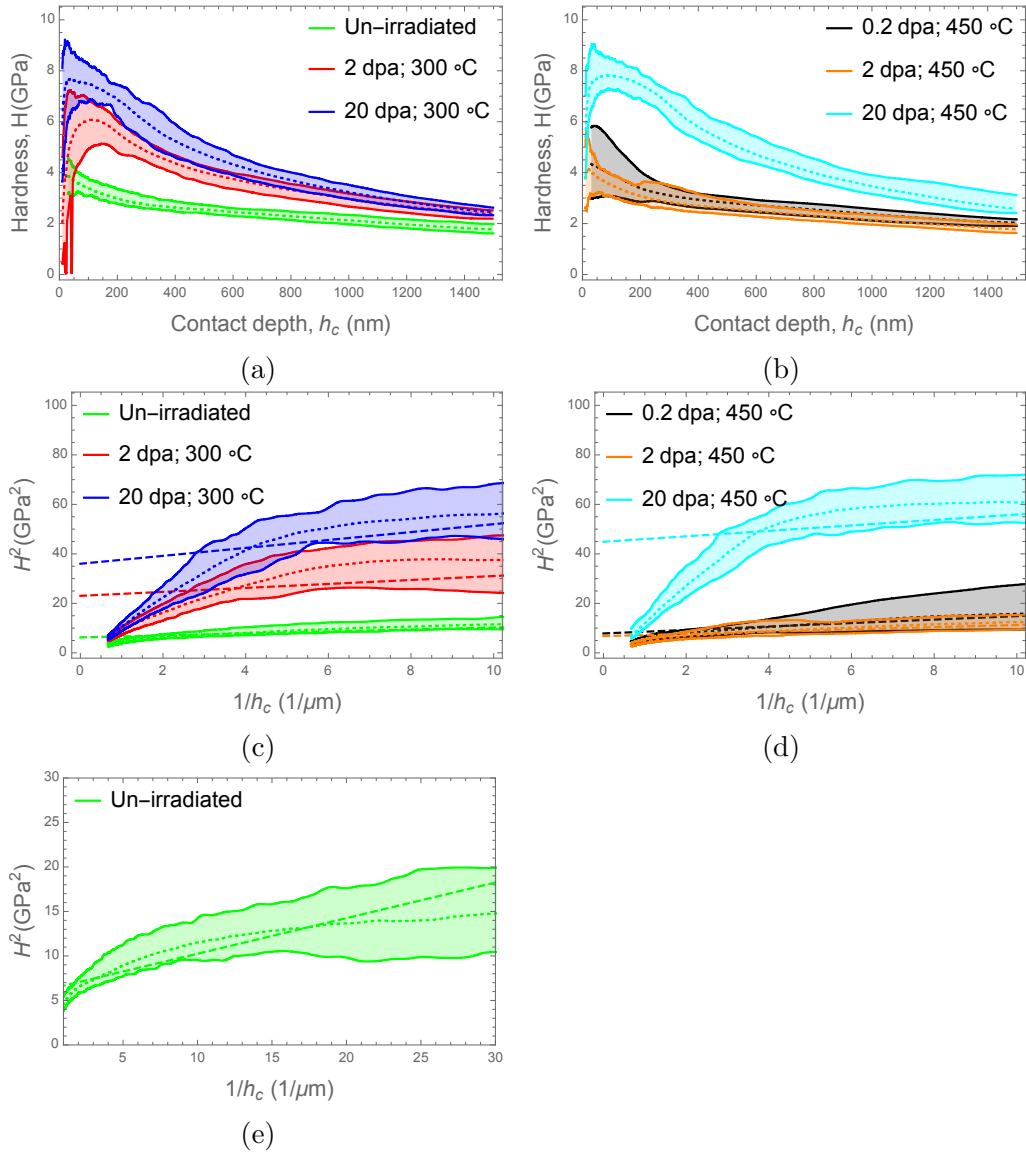
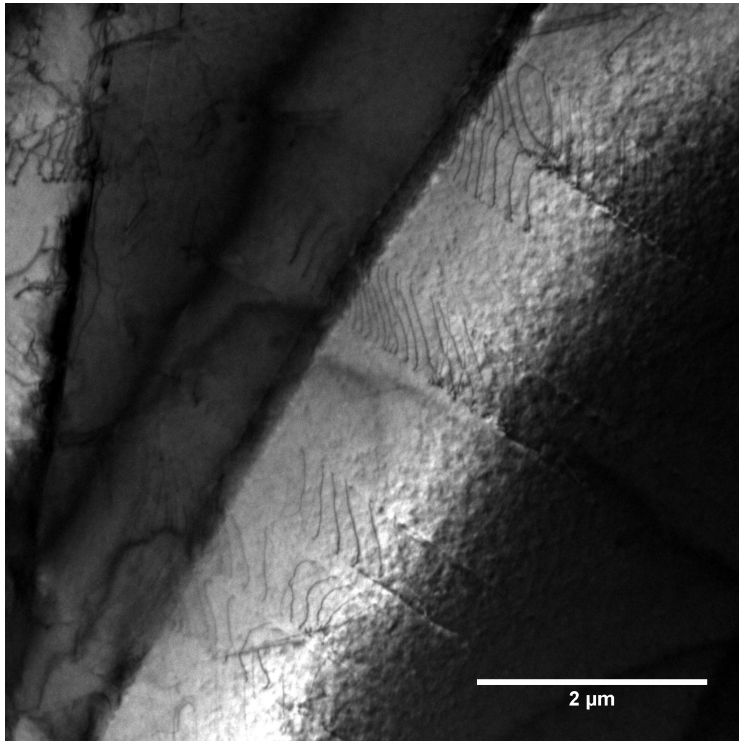
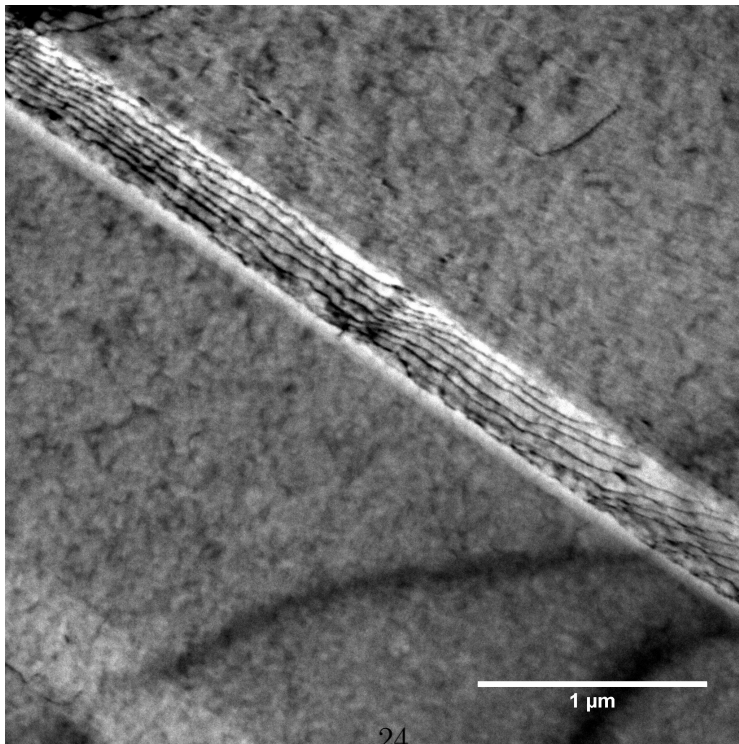


Figure 7: Hardness and hardness squared envelope plots, a)-b) and c)-d) respectively. The envelope is a consequence of the statistical spread from 25 indentations and CSM data per sample/condition.



(a)



24
(b)

Figure 8: TEM micrographs of the recrystallised condition. (a) for pile up of dislocations; (b) for slip band of dislocations